The Astrophysical Journal 885:144 13pp), 2019 November 10 https: doi.org 10.3847 1538-4357 ab4a00

Global Radiation Magnetohydrodynamic Simulations of sub Eddington Accretion Disks around Supermassive Black Holes

Yan-Fei Jiang)[1,2], Omer Blaes[3], James M. Stone[4], and Shane W. Davis[5]
[1] Kavli Institute for Theoretical Physics, Kohn Hall, University of California, Santa Barbara, CA 93106, USA
[2] Center for Computational Astrophysics, Flatiron Institute, New York, NY 10010, USA
[3] Department of Physics, University of California, Santa Barbara, CA 93106, USA
[4] Institute for Advanced Study, 1 Einstein Drive, Princeton, NJ 08540, USA
[5] Department of Astronomy, University of Virginia, P.O. Box 400325, Charlottesville, VA 22904-4325, USA
Received 2019 April 2; revised 2019 September 4; accepted 2019 September 30; published 2019 November 11

Abstract

We conduct global three-dimensional radiation magnetohydrodynamic simulations of the inner regions of accretion ows around a 5 × $10^8 M$ black hole, with mass accretion rates reaching 7 and 20 of the Eddington value. We choose initial field topologies that result in an inner disk supported by magnetic pressure, with surface density significantly smaller than the values predicted by the standard thin-disk model as well as a much larger disk scale height. The disks do not show any sign of thermal instability over many thermal timescales. More than half of the accretion is driven by radiation viscosity in the optically thin coronal region for the case of the lower accretion rate, while accretion in the optically thick part of the disk is driven by the Maxwell and Reynolds stresses from turbulence caused by magnetorotational instability. Optically thin plasma with gas temperatures 10^8 K is generated only in the inner ≈10 gravitational radii in both simulations, and is more compact in the case of the higher accretion rate. Such plasma does not form at larger radii because the surface density increases outward with radius, causing less dissipation outside the photosphere. In contrast to standard thin-disk models, the surface density in our simulations increases with increasing mass accretion rate at each radius. This causes a relatively weaker hot plasma component for the simulation with a higher accretion rate. We suggest that these results may provide a physical mechanism for understanding some of the observed properties of coronae and spectra of active galactic nuclei.

Key words: accretion, accretion disks – magnetohydrodynamics MHD) – methods: numerical – quasars: supermassive black holes – radiative transfer

1. Introduction

Active galactic nuclei AGNs) are believed to be powered by accretion onto supermassive black holes. The luminosity of most AGNs is observed to be smaller than the Eddington limit as defined by the electron scattering opacity, $L_{\rm Edd} = 1.5 \times 10^{46} M_{\rm BH}/(10^8 M_\odot)$ erg s ^{1}. The standard thin-disk model Shakura & Sunyaev 1973) has historically been widely used to describe the accretion ows in this regime when the AGN luminosity is larger than ≈0.01$L_{\rm Edd}$. The key assumptions in this model are that the disk is optically thick and supported by thermal pressure gas or radiation), and that the dissipation of gravitational binding energy is radiated away locally. The detailed disk structures in these models are determined by the famous assumption, which assumes that the stress responsible for the angular momentum transport in the disk is proportional to the thermal pressure.

There are numerous problems with the standard thin-disk model for AGNs, however, in terms of both theoretical self-consistency and its ability to match observations e.g., Koratkar & Blaes 1999; Antonucci 2013). The standard thin-disk model assumes a stationary ow, but is subject to thermal and in ow instabilities in the radiation pressure-dominated regime relevant to luminous AGNs Lightman & Eardley 1974; Shakura & Sunyaev 1976; Piran 1978). This should cause the disk to evolve away from the equilibrium state in a few thermal timescales Jiang et al. 2013a; Mishra et al. 2016) and probably show some kind of limit-cycle behavior Honma et al. 1991; Janiuk et al. 2002). However, this is not observed for most AGNs. The predicted ultraviolet continuum spectral energy distribution of this model is also not consistent with observations Zheng et al. 1997; Davis et al. 2007; Laor & Davis 2014), nor are predicted spectral features such as the Lyman edge Sincell & Krolik 1997; Shull et al. 2012; Tilton et al. 2016). Balmer absorption edges have been observed, however, through spectropolarimetric techniques Kishimoto et al. 2004).

The standard thin-disk model assumes that thermal pressure gas or radiation) is dominant in the disk. An alternative possibility that the vertical component of gravity in the accretion disk is primarily balanced by magnetic pressure has been proposed Shibata et al. 1990; Pariev et al. 2003). Begelman & Pringle 2007) studied the structure and stability of magnetic pressure-dominated disks by assuming that the toroidal magnetic fields will saturate to a level so that the associated Alfvén velocity reaches $\sqrt{c_s V_k}$ Pessah & Psaltis 2005; Das et al. 2018), where c_s is the gas sound speed and V_k is the disk rotation speed. Amplification of magnetic fields near the disk midplane is thought to be balanced by the escape of magnetic fields away from the midplane due to buoyancy. This magnetic elevated model is found to have a larger pressure scale height and is not subject to the radiation pressure-driven thermal and in ow instabilities that plague the standard model Sadowski 2016). This has interesting implications for both X-ray binaries and AGNs Begelman et al. 2015; Begelman & Silk 2017; Dexter & Begelman 2019). It is known that large-scale poloidal or radial magnetic fields are required in order to reach the magnetic pressure-dominated state Salvesen et al. 2016a, 2016b; Fragile & Sadowski 2017). One unusual

physical property that appears to be characteristic of global simulations of magnetically dominated ows is that mass accretion occurs predominantly in the surface layers of the disk Zhu & Stone 2018; Mishra et al. 2019). However, further work is needed beyond the pioneering simulations of Sadowski 2016) to understand how the strong radiation pressure in AGN accretion disks affects the disk structure in these magnetically elevated models.

An additional problem with standard disk models of AGNs is that their effective temperature typically $\sim 10^4$–10^5 K) is too low to explain the widely observed hard X-rays by direct thermal emission. It has been proposed that a high-temperature "corona," by analogy to the solar corona, is formed on top of the accretion disk Bisnovatyi-Kogan & Blinnikov 1976; Haardt & Maraschi 1991, 1993; Svensson & Zdziarski 1994; Zdziarski et al. 1999). The hot electrons in the corona produce X-rays by inverse Compton scattering of soft seed photons emitted by the disk, and the corona is inferred to occupy a compact region very near the black hole $\sim$10 gravitational radii, Reis & Miller 2013; Uttley et al. 2014). The amount of X-rays that can be produced via this mechanism compared with the thermal emission from the disk is determined by the fraction of accretion power that is dissipated in the coronal region. However, this fraction is a free parameter in these models because the actual mechanism that physically forms the corona, as well as the dependence of coronal properties on the parameters governing the accretion ow in AGNs, is unknown.

Early isothermal simulations of turbulence caused by magnetorotational instability MRI) in a local patch of a vertically stratified accretion disk Miller & Stone 2000) found that magnetic fields amplified near the disk midplane buoyantly rise to the surface, where they produce a magnetic pressure-dominated low-density region. This has long been suspected to be a mechanism for forming a corona. However, most local simulations that self-consistently determine the temperature of the plasma based on turbulent dissipation and radiative cooling typically find that the magnetic pressure-dominated upper layers are not heated to very high temperatures because of insufficient dissipation Blaes et al. 2007, 2011; Krolik et al. 2007; Hirose et al. 2009; Jiang et al. 2013a, 2016). An exception is Jiang et al. 2014b), who showed that the amount of dissipation in the magnetic pressure-dominated region can be increased by reducing the surface density of the disk, and this can substantially increase the plasma temperature outside the disk photospheres. The surface density is a free parameter in these local shearing box simulations, and the value required to produce the high-temperature corona is smaller than standard disk models would predict for the same accretion rate. It is therefore necessary to use global simulations to determine the surface density of the disk as well as the properties of coronae self-consistently for a given mass accretion rate.

There have been numerous studies trying to understand the properties of accretion disks with accretion rate below the Eddington limit based on global magnetohydrodynamic MHD) simulations e.g., Hawley 2001; Hawley & Krolik 2001; Ohsuga 2006; Shafee et al. 2008; Noble et al. 2009; Schnittman et al. 2013; Hogg & Reynolds 2016, 2018; Morales Teixeira et al. 2018). Most of these simulations do not include proper radiation transport except Morales Teixeira et al. 2018, where M1 closure is used) and instead adopt a cooling function to maintain a small ratio between the disk scale height and radius. This is in contrast to much thicker disks in quite different regimes of accretion rate see the review by Yuan & Narayan 2014). Such cooling functions necessarily preclude the formation of high-temperature coronae on top of the thin disks, although post-processing can be done to model the corona Schnittman et al. 2013).

Here we present the results of two global MHD simulations of sub-Eddington AGN accretion disks with self-consistent radiative transfer. Our work differs from many previous radiation MHD simulations of black hole accretion in that we have chosen parameters relevant to supermassive black holes rather than those of $\sim 10\,M$ e.g., McKinney et al. 2014; Mishra et al. 2016; Sádowski & Narayan 2016). This means that our disks are in the range where the ratios of radiation to gas pressure are substantially larger and opacities due to atomic transitions may be important. Our simulations form a disk in a region that is initially vacuum by accreting plasma from larger radius, with the advantage that the levels of gas, radiation, and magnetic pressure in the disk all arise from the physics of the simulations, as do the stresses transporting angular momentum. While the disks we study here depend on the assumed magnetic field strength and topology in the initial condition at large radius, the disks nevertheless form self-consistently. This contrasts with previous work that initialized the simulation with a standard thin-disk model in order to study its long-term evolution Fragile et al. 2018).

One goal of this work is to study the conditions under which dissipation of accretion occurs in optically thin regions a possible mechanism for the observed corona), and to study the dependence of its properties on parameters such as accretion rate. Another goal is to begin studying the possible role of radiation viscosity in this regime dominated by high radiation pressure Loeb & Laor 1992) with a simulation that is capable of tracking the angular dependence of the radiation intensity. Finally, we also include here realistic AGN opacities. Jiang et al. 2016) have shown that for typical densities and temperatures expected for AGN accretion disks based on the standard thin-disk model, the Rosseland mean opacity should be larger than the electron scattering value due to the so-called iron opacity peak. The density and temperature dependences of this peak can modify the thermal stability and structure of AGN accretion disks significantly. However, the local shearing box simulations done by Jiang et al. 2016) adopted a surface density given by the standard thin-disk model. Whether this opacity peak will show up or not depends on the actual disk structure that results from the physics in our simulation. We include a full opacity table in the simulations to capture its potential importance. As we shall see, the opacity effects turn out to not be so important in the two simulations we present here, but there are interesting levels of dissipation in optically thin regions as well as interesting levels of radiation viscosity.

The remainder of this paper is organized as follows. In Section 2, we describe the simulation setup. Detailed structures of the disk are described in Section 3. We discuss the implications of our simulations in Section 4.

2. Simulation Setup

We solve the same set of ideal MHD equations coupled with the time-dependent radiative transfer equation for specific intensities as in Jiang et al. 2019) using the code Athena J. M. Stone et al. 2019, in preparation). An approximate treatment of Compton scattering is included based on the difference between radiation temperature and gas temperature

Table 1
Simulation Parameters

Variables Units	AGN0.2	AGN0.07
r_i/r_g	80	80
ρ_i ρ_0	1	1
T_i/T_0	3.18	3.18
$\langle P_r/P_g\rangle$	4.47×10^5	4.61×10^5
$\langle P_r/P_g\rangle_\rho$	4.40×10^2	4.39×10^2
$\langle P_B/P_g\rangle$	1.27×10^{2}	2.32×10^{4}
$\langle P_B/P_g\rangle_\rho$	7.70×10^{3}	7.32×10^{5}
r r	6.1×10^{3}	6.1×10^{3}
θ	6.1×10^{3}	6.1×10^{3}
	6.1×10^{3}	6.1×10^{3}
N_n	80	80

Note. The center of the initial torus is located at r_i with density ρ_i and temperature T_i. The fiducial density and temperature are $\rho_0 = 10^{-8}$ g cm^{-3} and $T_0 = 2 \times 10^5$K. For any quantity a, $\langle a\rangle$ is the volume-averaged value over the torus while $\langle a\rangle_\rho$ is the averaged value weighted by the mass in each cell. The grid sizes Δr, $\Delta\theta$, $\Delta\phi$ are for the finest level at the center of the torus. The number of propagation directions for the radiation grid is N_n in each cell.

Jiang et al. 2019). We carry out two simulations, AGN0.2 and AGN0.07, for an $M_{\rm BH} = 5 \times 10^8 M_\odot$ black hole with accretion rates smaller than the Eddington value $\dot{M}_{\rm Edd} \equiv 10L_{\rm Edd}/c^2 = 8.22 \times 10^{26}$ g s^{-1}. The simulations are performed with the pseudo-Newtonian potential Paczy sky & Wiita 1980) $\phi = -GM_{\rm BH}/(r - 2r_g)$ to mimic the effects of general relativity around a Schwarzschild black hole, where G is the gravitational constant and $r_g \equiv GM_{\rm BH}/c^2 = 7.42 \times 10^{13}$ cm is the gravitational radius. We initialize a torus centered at $80r_g$ with the maximum density $\rho_0 = 10^{-8}$ g cm^{-3} and temperature $3.18T_0$, where $T_0 = 2 \times 10^5$ K. The shape of the torus is the same as that used in Jiang et al. 2019). The inner edge of the torus is at $40r_{\rm g}$ and the region inside that radius is filled with a density oor of $10^{9}\rho_0$ initially. The initial properties of the torus, including the ratios between the averaged radiation pressure P_r, gas pressure P_g, and magnetic pressure P_B, are summarized in Table 1. The main difference between the two simulations is the initial magnetic field in the torus. The run AGN0.2 uses a single loop of poloidal magnetic field while the run AGN0.07 adopts multiple magnetic field loops as described in Jiang et al. 2019). The different setups lead to different mass accretion rates in the disks that are formed near the black hole.

We use four levels of static mesh refinement to cover the whole simulation domain $(r, \theta, \phi) \in (4r_g, 1600r_g) \times (0, \pi) \times (0, 2\pi)$. The level with the highest resolution reaches $\Delta r/r = \Delta\theta = \Delta\phi = 6.1 \times 10^{-3}$ for the region $(6r_g, 200r_g) \times (1.48, 1.66) \times (0, 2\pi)$, which covers most of the mass near the disk midplane. The equivalent resolution is $1024 \times 512 \times 1024$, which is necessary to resolve these sub-Eddington accretion disks.

We use 80 discrete angles in each cell to resolve the angular distribution of the radiation field, which is in thermal equilibrium initially in the torus. We calculate the Rosseland mean opacity in each cell by using local density and temperature based on the OPAL opacity table with solar metallicity Paxton et al. 2013; Jiang et al. 2015). Planck mean free–free absorption opacity is also included as $3.7 \times 10^{53}(\rho^9 E_g^7)^{1/2}$, where E_g is the gas internal energy.

3. Results

3.1. Resolution for MRI

To quantify how well the MRI is resolved in our simulations, we calculate the quality factors Q_θ and Q , which are the ratios between the wavelength of the fastest growing MRI mode $\lambda = 2\pi\sqrt{16/15}\,|v_{\rm A}|/\Omega$ and cell sizes $r\Delta\theta$, $r\sin\theta\Delta\phi$ along the θ and directions, where the Alfvén velocity $v_{\rm A}$ is calculated for B_θ and B respectively. Resolution studies for non-radiative ideal MHD simulations Hawley et al. 2011; Sorathia et al. 2012) find that when $Q_\phi \gtrapprox 25$, $Q_\theta \gtrapprox 6$, or both Q and Q_θ are larger than 10, properties of MRI turbulence converge with respect to resolution. Although there is no general criterion on the convergence of radiation MHD simulations of accretion disks, we use this as a way to compare our resolutions with these calculations. We calculate the azimuthally averaged quality factors during the final turbulent states for both of the calculations. For the simulation AGN0.07 at the disk midplane, $Q = 100$ at $r = 5r_g$ and it decreases to 80 at $r = 30r_g$, while Q_θ varies from 10 to 8 in the same radial range. For a fixed radius, the combined effects of increasing Alfvén velocity and reduced resolution with height from the disk midplane cause the quality factors to decrease by a factor of $\approx$2 at the photosphere. For the simulation AGN0.2, the quality factors are larger as the disk is thicker. The midplane Q changes from 200 at $5r_g$ to 40 at $40r_g$ while Q_θ changes from $\approx$20 to $\approx$10 between $5r_g$ and $40r_g$ at the disk midplane. For this run, the quality factors increase by a factor of $\approx$2 from the midplane to the photosphere. The resolutions are therefore sufficient to resolve the MRI turbulence according to the criterion found by non-radiative MHD simulations. This is possible for these sub-Eddington accretion disks because magnetic pressure is the dominant pressure, which makes the wavelength of the fastest growing MRI mode comparable to the disk scale height and easier to resolve.

3.2. Simulation Histories

Gas in the initial torus ows toward the black hole, and the accretion disk is slowly built up. Histories of the mass accretion rate $\dot{M} \equiv \int_0^{2\pi}\int_0^{\pi} \rho v_r r^2 \sin\theta d\theta d\phi$ at $10r_g$ for the two runs are shown in the left panel of Figure 1. After an initial transient period, the simulation AGN0.07 reaches an accretion rate $7\%\dot{M}_{\rm Edd}$ when averaged after time $t = 2.4 \times 10^4 r_g\ c$. For the run AGN0.2, the averaged accretion rate is $22\%\dot{M}_{\rm Edd}$ after $t = 3 \times 10^4 r_g\ c$. All the analyses for the time-averaged properties of the two simulations are also performed for the same time intervals. The mass accretion rates show significant uctuations due to turbulence. The standard deviation of $\dot{M}$ during the steady state for the run AGN0.07 is only 1.2 of the averaged value while the corresponding value is 12.3 for the run AGN0.2. The main difference in the two simulations is the magnetic field topology as described in Section 2. The run AGN0.2 adopts a single loop of magnetic field in the initial torus and there are net poloidal magnetic fields $\overline{B}_\theta$ through the inner region of the disk. The ratio between radiation pressure and $\overline{B}_\theta^2/2$ near the disk midplane is $\approx 10^3$. For the run AGN0.07, quadrupole magnetic fields are used in the initial condition, which result in net radial magnetic fields $\overline{B}_r$ near the disk midplane, although the shell-averaged B_r across the whole disk is still zero. The net $\overline{B}_r$ near the disk midplane is sheared into toroidal magnetic field within an orbital timescale and quickly builds up strong magnetic pressure, which then escapes

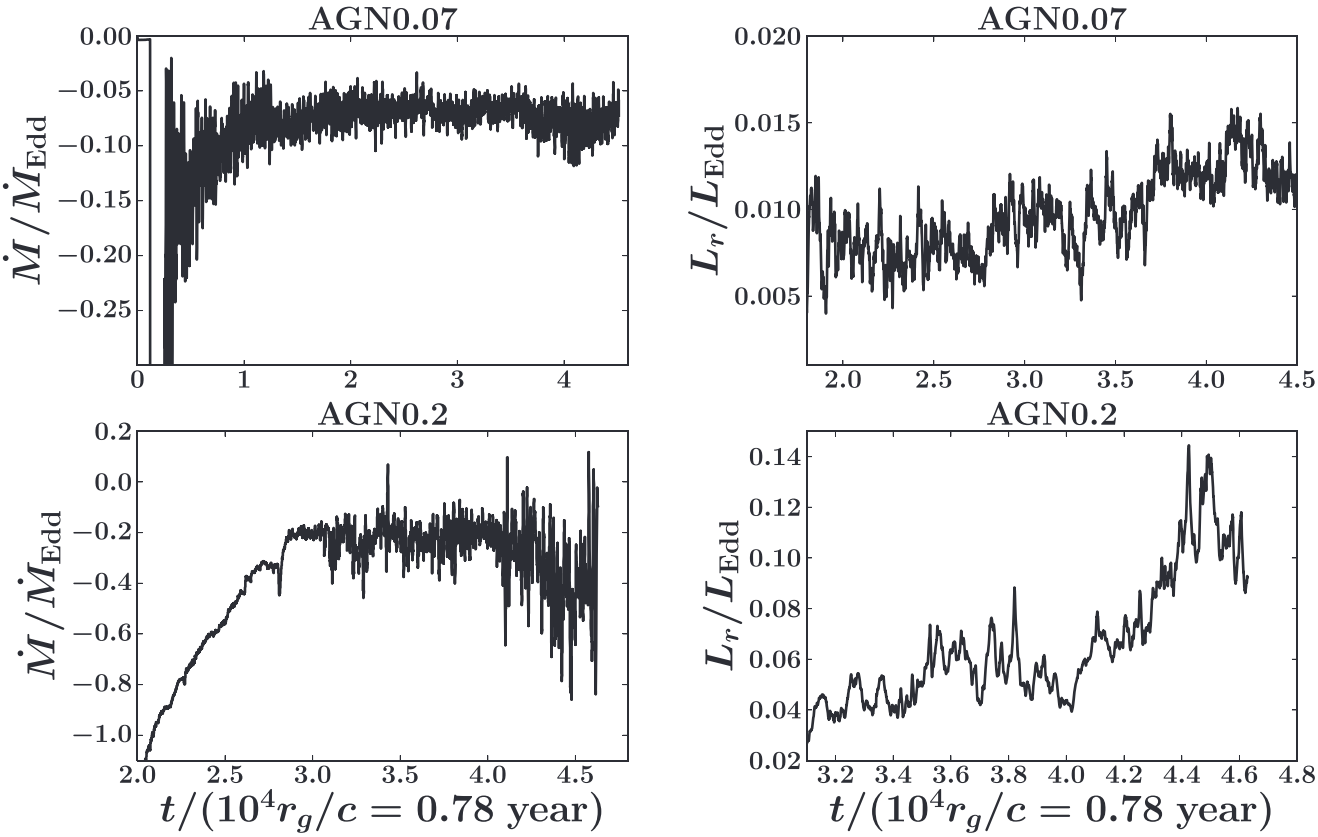

Figure 1. Left: histories of the net mass accretion rate negative values for in ow) at $10r_g$ for the two simulations AGN0.07 top panel) and AGN0.2 bottom panel). The total durations of the simulations correspond to more than 10 thermal timescales at $10r_g$. Right: histories of total radiative luminosity emitted within the cylindrical radius $10r_g$ of the disk for simulations AGN0.07 top panel) and AGN0.2 bottom panel). Note that the horizontal axes have different offsets in the panels.

from the midplane due to buoyancy. MRI turbulence still develops in this case Pessah & Psaltis 2005; Das et al. 2018), but it shows less variability than the other run. Detailed investigations of magnetic pressure-dominated disks resulting from this magnetic field configuration are described in Section 3.3.

In most MHD simulations of accretion disks where radiative transfer is not calculated self-consistently, density or stress is usually used as the proxy to understand the observed properties of these systems. Since our simulations calculate the photons emitted by the disk directly, we can calculate the frequency-integrated light curves for the timescale that our simulations can cover. In order to avoid contamination from photons generated by the torus at large radii where the disk has not reached a steady state, we convert the radiation ux $\boldsymbol{F}_r$ to the radial and vertical components, F_R and F_z, in cylindrical coordinates and then integrate the total radiative luminosity that leaves the cylindrical surface at $R = 10r_g$ and height $z = 100r_g$, which is well beyond the photosphere. The resulting light curves are shown in the right column of Figure 1 and have much weaker short-timescale variations than the variability in $\dot{M}$. This is likely due to the scattering of photons through the optically thick disks. Indeed, the power spectrum of the light curve from the run with a lower accretion rate AGN0.07) has more power at high frequencies than that from the run with a higher accretion rate AGN0.2). This is because the midplane optical depth increases with increasing mass accretion rate see Figure 6). The changes of variability amplitude with luminosity are also different in the two light curves, revealing different dynamo actions in the disk, which will be discussed in Section 4.

Histories of the poloidal profiles of azimuthally averaged density ρ, gas temperature T_g, and toroidal magnetic field B at $10r_{\rm g}$ for the two runs are shown in Figure 2. The disk photosphere only extends to $\approx 6^\circ$ away from the disk midplane for the run AGN0.07, while it covers more than 14° in the simulation AGN0.2. Once above the photosphere, as indicated by the blue lines in the top panels, gas temperature increases rapidly to $\approx 10^9$ K. We label this the "corona" region, although whether and how this might be related to the observationally inferred corona in AGNs will be discussed below in Section 3.6. In the optically thick part of the disk, gas and radiation are in thermal equilibrium with a temperature around 10^5 K. The grid-scale variation of gas temperature is unrealistic because the gas pressure is smaller than 0.1 of the radiation and magnetic pressures and it suffers from numerical noise. The toroidal magnetic field switches sign near the disk midplane after $\approx 10^4 r_g\ c$ for the run AGN0.2, which creates the well known butter y diagram caused by the MRI dynamo Stone et al. 1996; Miller & Stone 2000; Davis et al. 2010; O Neill et al. 2011; Simon et al. 2012; Jiang et al. 2013a, 2014a). This does not happen for the run AGN0.07, although MRI turbulence has also developed there. This is because shearing of the net radial magnetic field near the disk midplane for the run AGN0.07 always forms B with the same sign in addition to the B generated by MRI see Section 3.5).

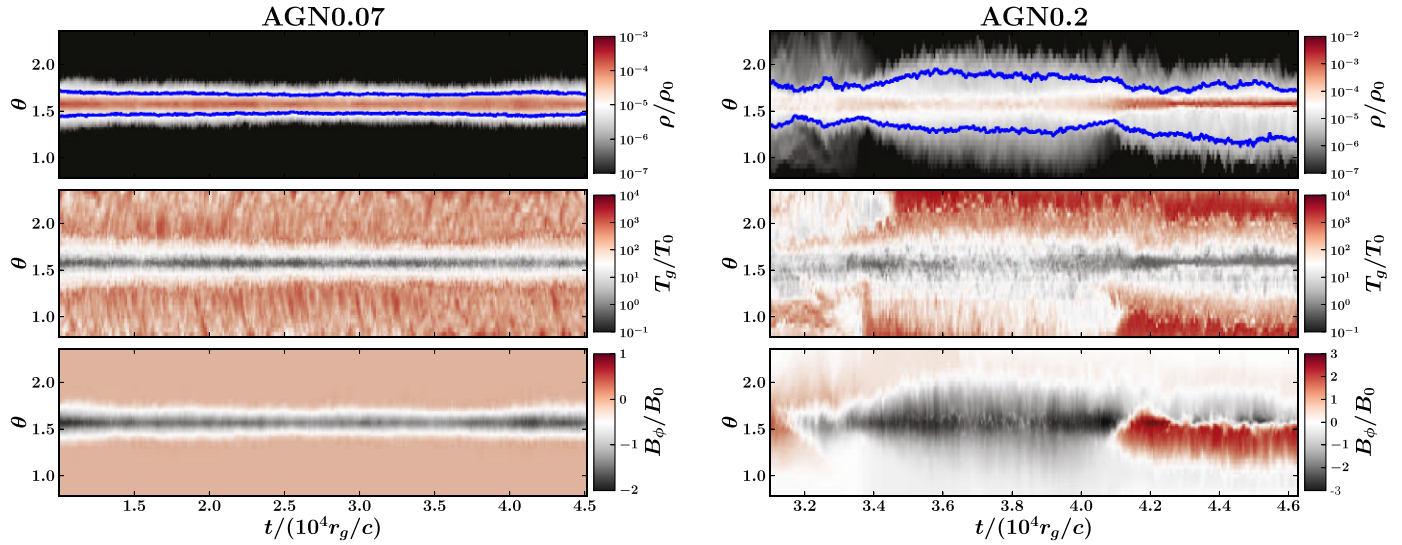

Figure 2. Space–time diagrams for the histories of azimuthally averaged density ρ in units of $\rho_0 = 10^{-8}$ g cm^{-3}, top panels), gas temperature T_g in units of $T_0 = 2 \times 10^5$ K, middle panels), and toroidal magnetic field B in units of $B_0 = 1.87 \times 10^3$ G, bottom panels) at $10r_g$. The two columns are for the run AGN0.07 left) and AGN0.2 right). The blue lines in the top panel indicate the location where the optical depth for the Rosseland mean opacity measured along the polar $\pm\theta$) direction to the rotation axis is one.

3.3. Disk Structure

The time-averaged and azimuthally averaged spatial structures inside $30r_g$ for the density, ow velocity, radiation energy density, and magnetic field lines of the two simulations are shown in Figure 3. Radial profiles of different shell-averaged pressure components, the mass accretion rate, as well as the total optical depth are shown in Figures 4–6. The disk is thinner in the run AGN0.07 compared with AGN0.2 due to the lower accretion rate, but the thickness of the disk differs significantly from predictions of the standard accretion disk model. In an -disk model dominated by radiation pressure and electron scattering in a spherically symmetric gravitational potential, vertical hydrostatic equilibrium implies that the thickness of the disk is $H = [\kappa_s \dot{M}/(4\pi c)]|d \ln \Omega / d \ln r|$ away from the inner boundary. Near the inner boundary $r_{\rm in}$, it is smaller by a factor $1 - (r_{\rm in}/r)^{1/2}$. This is nearly independent of radius and of), and implies $H/r_g \approx 1.1$ Frank et al. 2002) for $\dot{M} = 7\%\dot{M}_{\rm Edd}$ and $H/r_g \approx 3.0$ for $\dot{M} = 20\%\dot{M}_{\rm Edd}$. It will be even smaller if we take into account the boundary effect. As shown in Figure 3, the heights of the photospheres clearly increase rapidly with radius in the two runs, and become larger than the values in the standard -disk model beyond $\approx 10r_g$. The contrast of radiation energy density inside and above the photosphere is much smaller in AGN0.07 than in the run AGN0.2 because of the reduced total optical depth as well as different spatial distributions of dissipation. Although the shell-averaged radiation pressure is still larger than or comparable to the magnetic pressure Figure 4), the vertical gradient of radiation pressure is actually smaller, particularly in the run AGN0.07. The disk is actually supported by the magnetic pressure gradient in this region Section 3.5). There are two magnetic field loops above and below the disk midplane in the run AGN0.07, and they are configured in such a way as to have a net radial magnetic field near the midplane. In the run AGN0.2, there are net poloidal magnetic fields threaded through the disk by design. We emphasize, however, that with both magnetic field configurations, the strong magnetic pressure is dominated by the turbulent component, since the magnetic pressure due to the azimuthally averaged mean magnetic field $\overline{B}^2/2$ is smaller than the total magnetic pressure by a factor of ≈ 10 Figure 4).

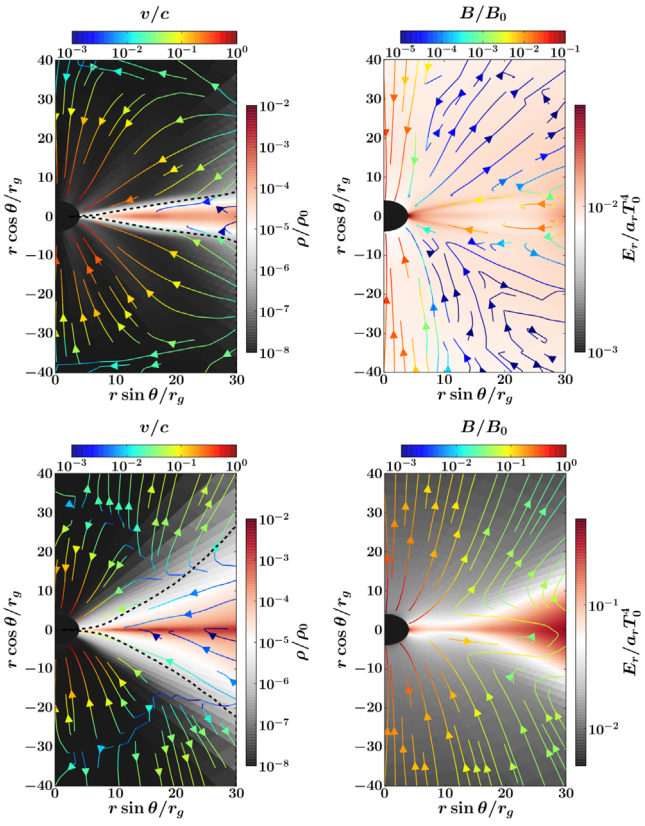

Figure 3. Time-averaged and azimuthally averaged spatial structures for the inner $40r_g$ of the disks from the two simulations, AGN0.07 top panels) and AGN0.2 bottom panels). The left column is for density the color) and ow velocity the streamlines) while the right column is for radiation energy density the color) and magnetic field lines the streamlines). The dashed black line in the left column indicates the location where the polar $\pm\theta$) optical depth to the rotation axis for Rosseland mean opacity is 1.

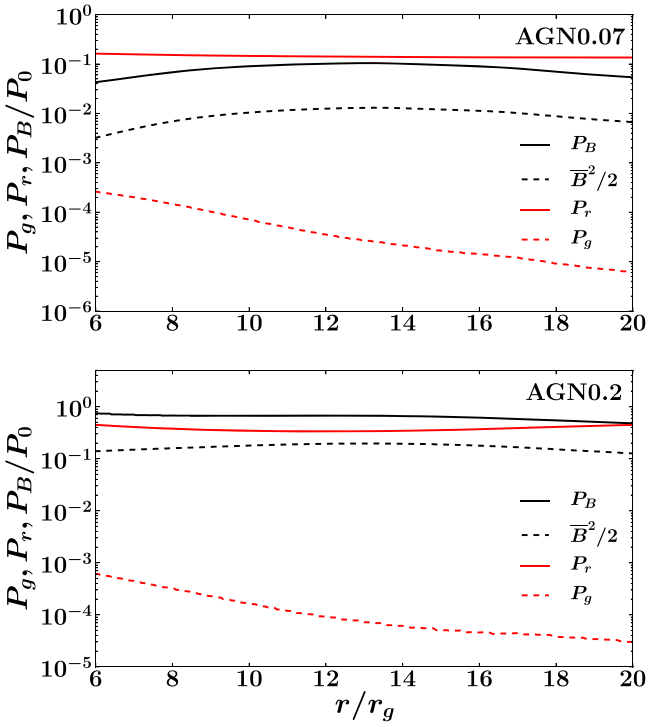

Figure 4. Radial profiles of the time- and shell-averaged gas pressure P_g, dashed red lines), radiation pressure P_r, solid red lines), total magnetic pressure P_B, solid black lines), and magnetic pressure due to the azimuthally averaged magnetic field $\overline{B}^2/2$, dashed black lines) in the two simulations AGN0.07 top panel) and AGN0.2 bottom panel).

Radial profiles of the mass accretion rate averaged over whole spherical shells and over time reach constant values inside $\approx 15 r_g$ for AGN0.07 and $\approx 13 r_g$ for AGN0.2 Figure 5). We decompose the net mass accretion rate into two parts based on the location of the photosphere shown in Figure 3. At each radius, we integrate $\rho v_r r^2$ for θ angles either above or below the photosphere, and radial profiles of the two components are shown in Figure 5 as red and dashed black lines, respectively. For the run AGN0.2, the majority of accretion happens in the optically thick part of the disk until $r < 7 r_g$. For the run AGN0.07, more than half of the mass is accreted in the optically thin surface of the disk over the entire radial range where the disk has reached a steady state. The spatial distribution of mass in ow is consistent with the location of stress for angular momentum transport Section 3.4). Significant surface accretion has also been found in non-radiative ideal MHD simulations of accretion disks with a net poloidal magnetic field Zhu & Stone 2018). In fact, the resulting magnetic field configuration from the run AGN0.2 shown in Figure 3 is very similar to that found by Zhu & Stone 2018) e.g., Figure 25 of that paper). The poloidal magnetic fields are advected inward above the disk midplane. Since we can determine the thermal properties of the disk self-consistently, for the accretion rate of $26\% \dot{M}_{\rm Edd}$, accretion still happens in the optically thick part of the disk with little accretion in the coronal region. When the accretion rate drops to 7 with a reduced optical depth, mass is primarily accreted in the optically thin region. However, for these AGN disks, the mechanism of angular momentum transport responsible for the coronal accretion is due to radiation instead of the magnetic stresses that dominate in non-radiative ideal MHD simulations Section 3.4).

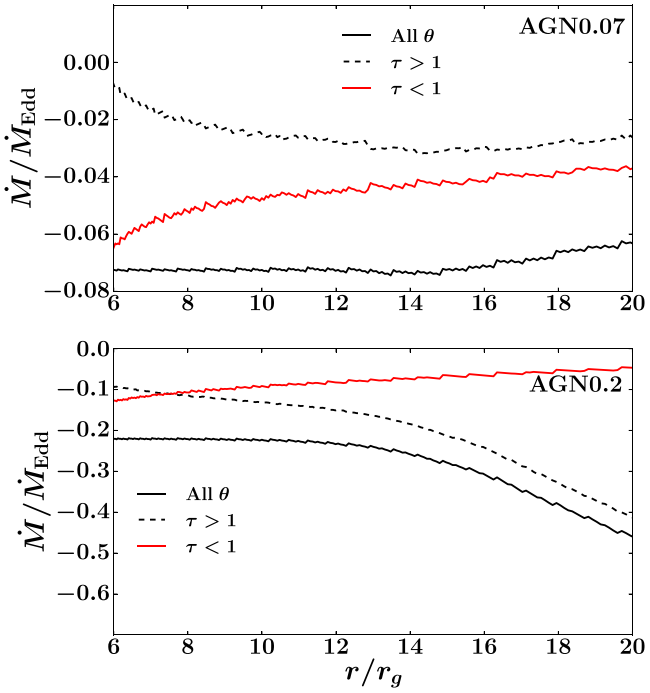

Figure 5. Radial profiles of the time-averaged net mass accretion rate $\dot{M}$ for the two runs AGN0.07 top panel) and AGN0.2 bottom panel). The solid black lines are $\dot{M}$ integrated over all polar angles, while the solid red and dotted black lines are $\dot{M}$ in the optically thin and thick regions respectively.

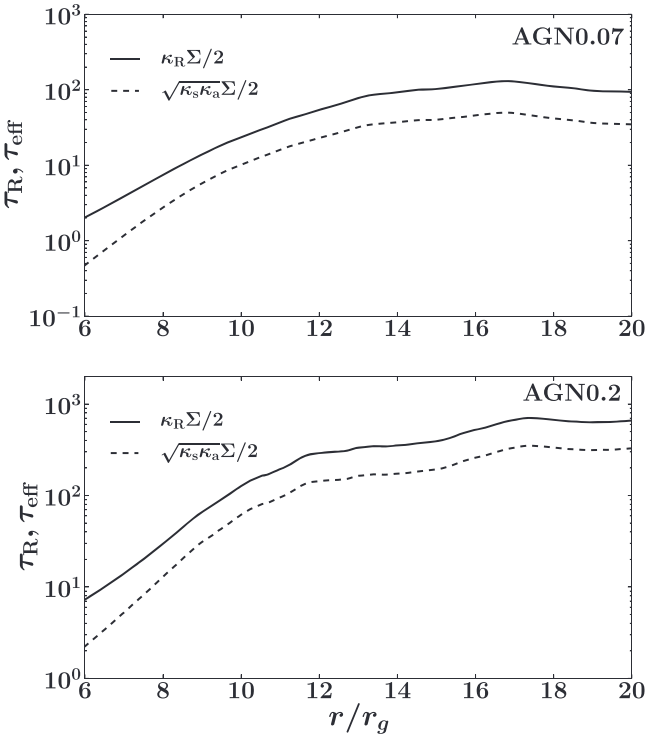

Figure 6. Radial profiles of the total Rosseland mean $\kappa_R \Sigma/2$) and effective absorption $\sqrt{\kappa_s \kappa_a}\Sigma/2$) optical depths from the disk midplane to the rotation axis. Here κ_a and κ_s are the absorption and scattering opacities while $\kappa_R \equiv \kappa_a + \kappa_s$ is the Rosseland mean opacity. The top and bottom panels are for the two runs AGN0.07 and AGN0.2 respectively.

Radial profiles of time-averaged Rosseland mean optical depth $\tau_R = \kappa_R \Sigma/2$ for the two runs are shown in Figure 6. Here the Rosseland mean opacity $\kappa_R \equiv \kappa_a$ κ_s is the sum of

absorption κ_a and scattering κ_s opacity. Optical depths for effective absorption $\tau_{\rm eff} = \sqrt{\kappa_s \kappa_a}\Sigma/2$ are also shown in the same figure. The Rosseland mean optical depth is only 2 at $6r_g$ for AGN0.07, and it increases to 100 at $14r_g$, while the effective absorption optical depth drops below 1 near the innermost stable circular orbit. When the accretion rate is increased to $26\%\dot{M}_{\rm Edd}$, the optical depth is increased by a factor of 2–3 and the entire disk is optically thick even for effective absorption. The optical depth in the disk is smaller than the prediction of the standard -disk model by a factor of ≈10 for the same mass accretion rate due to the increased disk scale height and in ow velocity because of strong magnetic pressure support Section 3.5).

3.4. Stresses for Angular Momentum Transport

In accretion disks, transport of angular momentum can be provided by the sum of Maxwell, Reynolds, and radiation the off-diagonal components of the radiation pressure) stresses. Since radiation pressure is so significant in AGN accretion disks, radiation stress can potentially play an important role as an effective viscosity Loeb & Laor 1992). In the optically thick regime, radiation viscosity is proportional to $E_r/(c\rho\kappa_R)$ multiplied by the shear rate of the velocity field Weinberg 1971; Mihalas & Mihalas 1984; Kaufman & Blaes 2016). If we only consider the shear rate for a Keplerian disk near the disk midplane, the ratio between the radiation stress and radiation pressure at radius r is $\sim\mathcal{O}(\sqrt{r_g/r}/(r\rho\kappa_R))$. For a standard model of a thin accretion disk where $r\rho\kappa_R \gtrapprox 100$, the radiation stress will be much smaller than the typical Maxwell and Reynolds stresses produced by MRI turbulence. In other words, radiation viscosity is small because the mean free path of the photons is too short. This is also true for super-Eddington accretion disks around AGNs due to their large optical depth Jiang et al. 2019), even though radiation pressure is significantly larger than the gas and magnetic pressure there. However, this is not the case for these sub-Eddington simulations.

Radial profiles of the shell-averaged Maxwell $_m$), Reynolds $_h$), and radiation stresses only the r– component remains, $_{\rm rad}$) scaled with the shell-averaged total pressure for the two runs are shown in Figure 7. The stresses are calculated in the same way as in Jiang et al. 2019). In their non-radiative global simulations of magnetically elevated disks with surface accretion layers, Mishra et al. 2019) found that accretion was largely driven by Maxwell stresses from coherent, large-scale magnetic fields. Surface accretion in the simulations by Zhu & Stone 2018) also appears to be driven by coherent Maxwell stresses. This differs from what we find here. The Maxwell stress due to the azimuthally averaged mean $\langle B_r\rangle$ and $\langle B_\phi\rangle$ fields for both simulations is shown as the dashed black lines in Figure 7. This is smaller than the total Maxwell stress by a factor of 2–3 in AGN0.2 and a factor of 2 in AGN0.07, despite the fact that the latter has shearing net radial magnetic field in the midplane. The total stress in the run AGN0.2 is dominated by the Maxwell stress, with the Reynolds and radiation stresses smaller by a factor of ≈5, which is consistent with the results reported by previous local and global simulations of MRI turbulence with net vertical magnetic fields Bai & Stone 2013; Zhu & Stone 2018). However, for the run AGN0.07, the radiation stress is larger than the others by more than a factor of 2 for all the radial range $r > 5r_g$, while the Maxwell and Reynolds stresses vary from 2 to 10 of the total pressure,

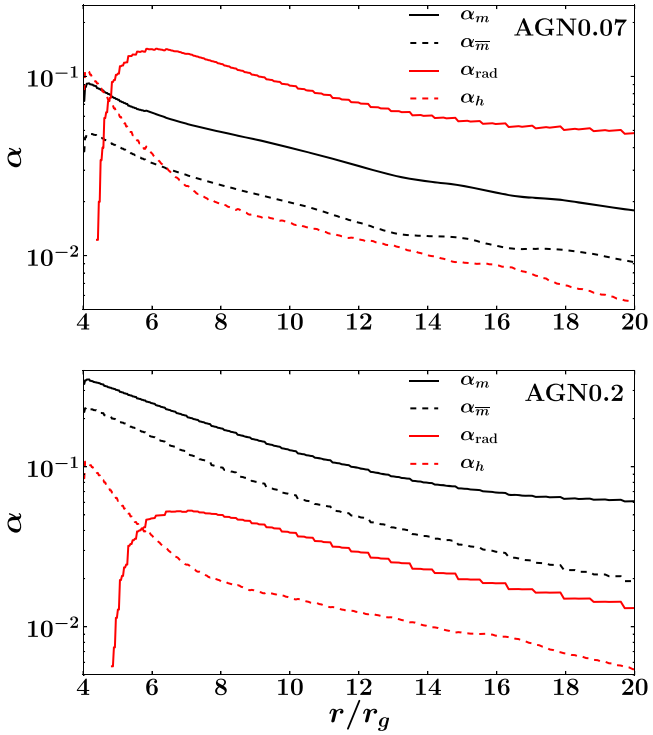

Figure 7. Radial profiles of the time- and shell-averaged ratios between Reynolds $_h$, dashed red lines), Maxwell $_m$, solid black lines), and radiation $_{\rm rad}$, solid red lines) stresses and total pressure for the runs AGN0.07 top) and AGN0.2 bottom). The dotted black lines $\alpha_{\overline{m}}$) are for stresses due to the azimuthally averaged mean $\langle B_r\rangle$ and mean $\langle B_\phi\rangle$.

which are typical values found by MRI turbulence without net vertical magnetic fields Hawley et al. 1995; Miller & Stone 2000; Hirose et al. 2006; Davis et al. 2010; Jiang et al. 2013a, 2014b).

Radiation stress and Maxwell stress dominate different locations of the disk in the run AGN0.07 because they have different spatial distributions. The time-averaged and azimuthally averaged spatial distributions of the r– and θ– components of radiation stress, $P_r^{r\phi}$ and $P_r^{\theta\phi}$, for the run AGN0.07 are shown in the first two panels of Figure 8. For comparison, the Maxwell stress S_m and Reynolds stress S_h are shown in the third and fourth panels. Inside the photosphere of the disk, the radiation stress is actually much smaller than the Maxwell and Reynolds stresses. This is consistent with our estimate that radiation stress is proportional to 1 $r\rho\kappa_R$), while the Maxwell and Reynolds stresses roughly follow the distribution of mass. However, once near the photosphere, because of the increased photon mean free path as well as the large velocity gradient, significant radiation stress is present while the Maxwell and Reynolds stresses drop significantly. This suggests that in the run AGN0.07, angular momentum is transported by the Maxwell and Reynolds stresses in the optically thick part of the disk. But once near the photosphere, angular momentum is transported by the radiation stress. Since total radiation stress dominates, more accretion happens in the optically thin region, which is consistent with the mass accretion rates shown in Figure 5. This is not the case for the run AGN0.2, where most accretion still happens in the optically thick region until $r \lessapprox 8r_g$. This also causes a stronger coronal component at large radii for the run AGN0.07 Section 3.6), since dissipation associated with the accretion

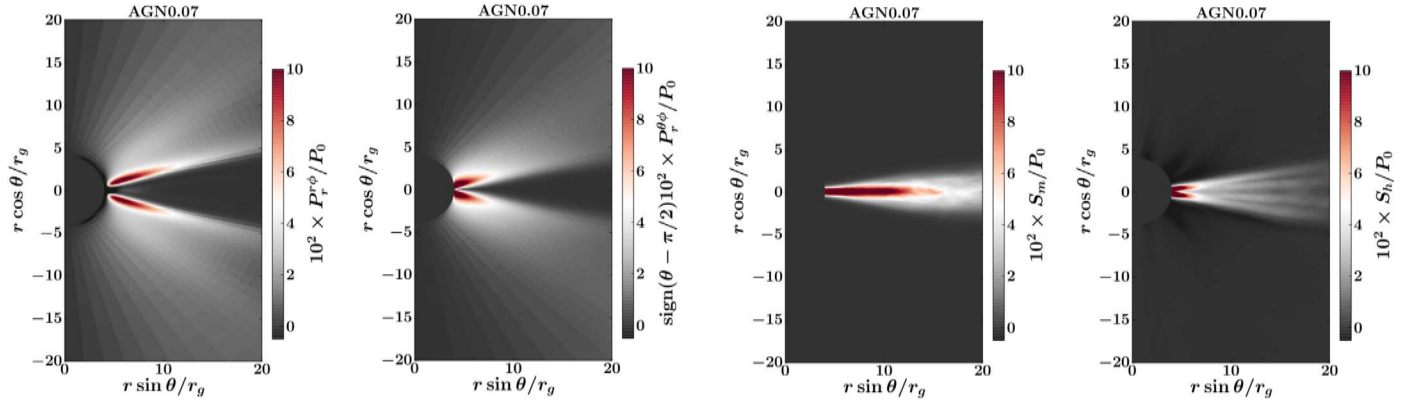

Figure 8. Time-averaged and azimuthally averaged spatial distributions for the off-diagonal components of radiation pressure $P_r^{r\phi}$ the first panel) and $P_r^{\theta\phi}$ the second panel) for the run AGN0.07. We add a negative sign to $P_r^{\theta\phi}$ above the disk midplane so that it can be compared with other stress components easily with the same color scheme. The third and fourth panels are the corresponding Maxwell and Reynolds stresses for comparison.

in the optically thin region can heat up the gas easily without cooling efficiently.

The amount of radiation stress we observe in the simulations can also be compared with analytic expectations for radiation viscosity. When the optical depth per cell is large, the r– component of the comoving frame radiation viscosity can be calculated analytically as Masaki 1971; Kaufman & Blaes 2016)

$$P^{r\phi}_{r,\mathrm{vis}} = -\frac{8}{27}\frac{E_r}{\rho\kappa_R c}D_{r\phi}, \tag{1}$$

where the r– shear rate in spherical polar coordinates is $D_{r\phi} = r\partial(v_\phi/r)/\partial r \quad 1/(r\sin\theta)\partial v_r/\partial\phi$. However, when cells become optically thin, this formula needs to be modified to account for the nonzero mean free path of photons. Under optically thin conditions, the viscous stress tensor associated with a shear velocity difference across some given length scale should be proportional to the optical depth across that scale times the velocity difference Socrates et al. 2004; Kaufman & Blaes 2016). As a crude estimate that bridges the optically thin and thick regimes, we therefore write the stress tensor as

$$P^{r\phi}_{r,\mathrm{vis}} = -\frac{8E_r}{27c}k(\tau)D'_{r\phi}. \tag{2}$$

Here $D'_{r\phi} \equiv r\Delta(v_\phi/r) + \Delta v_r$ is just the difference in shear rate across distances with optical depth τ along radial for v) and azimuthal for v_r) directions, and $k(\tau) = \tau^{-1}$ for $\tau > 1$ and τ for $\tau < 1$. In practice, we first determine the optical depth per cell at each location. If that value is larger than one, we calculate the difference in shear rate between neighboring cells. If that value is smaller than 1, we extend the distance until $\tau = 1$ is reached and calculate the difference in shear rate there. The radiation stress tensor calculated based on the above formula is transformed back to the lab frame and then averaged azimuthally to compare with the r– radiation stress returned by the simulations directly. Comparisons for two different radii are shown in Figure 9. The numerically calculated radiation stress nicely follows the prediction for radiation viscosity in the optically thick regime and roughly follows our order-of-magnitude estimate in the optically thin regime. The biggest discrepancy near the photosphere is likely due to the fact that our estimate Equation 2)) was designed only to bridge the optically thick and thin limits and is therefore least accurate for $\tau \approx 1$.

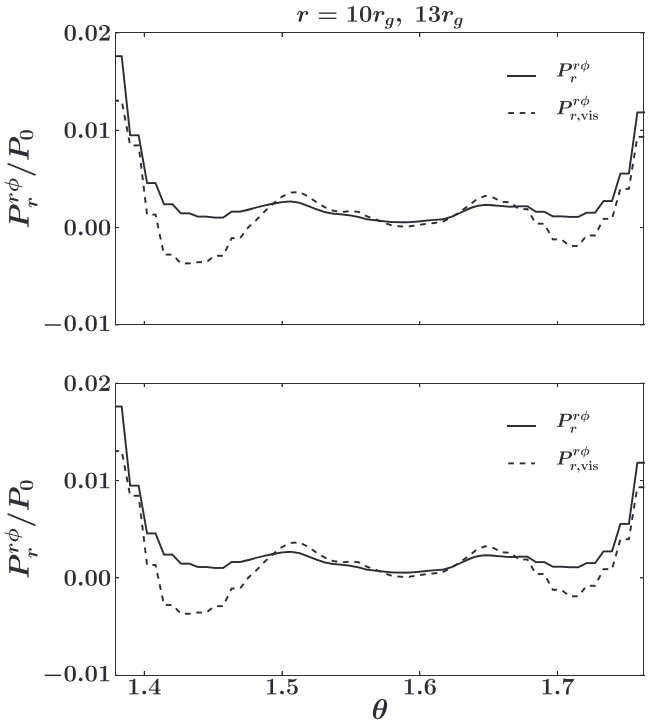

Figure 9. Comparison between the vertical profiles of the azimuthally averaged radiation stress $P_r^{r\phi}$ solid lines) calculated by the simulation AGN0.07 and with the analytical formula for radiation viscosity $P_{r,\mathrm{vis}}^{r\phi}$ dashed lines), based on Equations 1) and 2). The top and bottom panels are for radii $10r_g$ and $13r_g$ respectively. This comparison is done for the snapshot at time $4.5\times10^4 r_g\ c$. The photosphere is located at $\theta = 1.47$ and $\theta = 1.67$ for the top and bottom portions of the disk.

3.5. Vertical Structure of the Disk

Time-averaged and azimuthally averaged poloidal profiles of various quantities at $10r_g$ for the two runs are shown in Figure 10. The density drops faster with height in the run AGN0.07 due to a smaller pressure scale height. Shapes of density profiles are also more centrally peaked than those of disks dominated by gas or radiation pressure found by both local shearing box and global simulations Turner 2004;

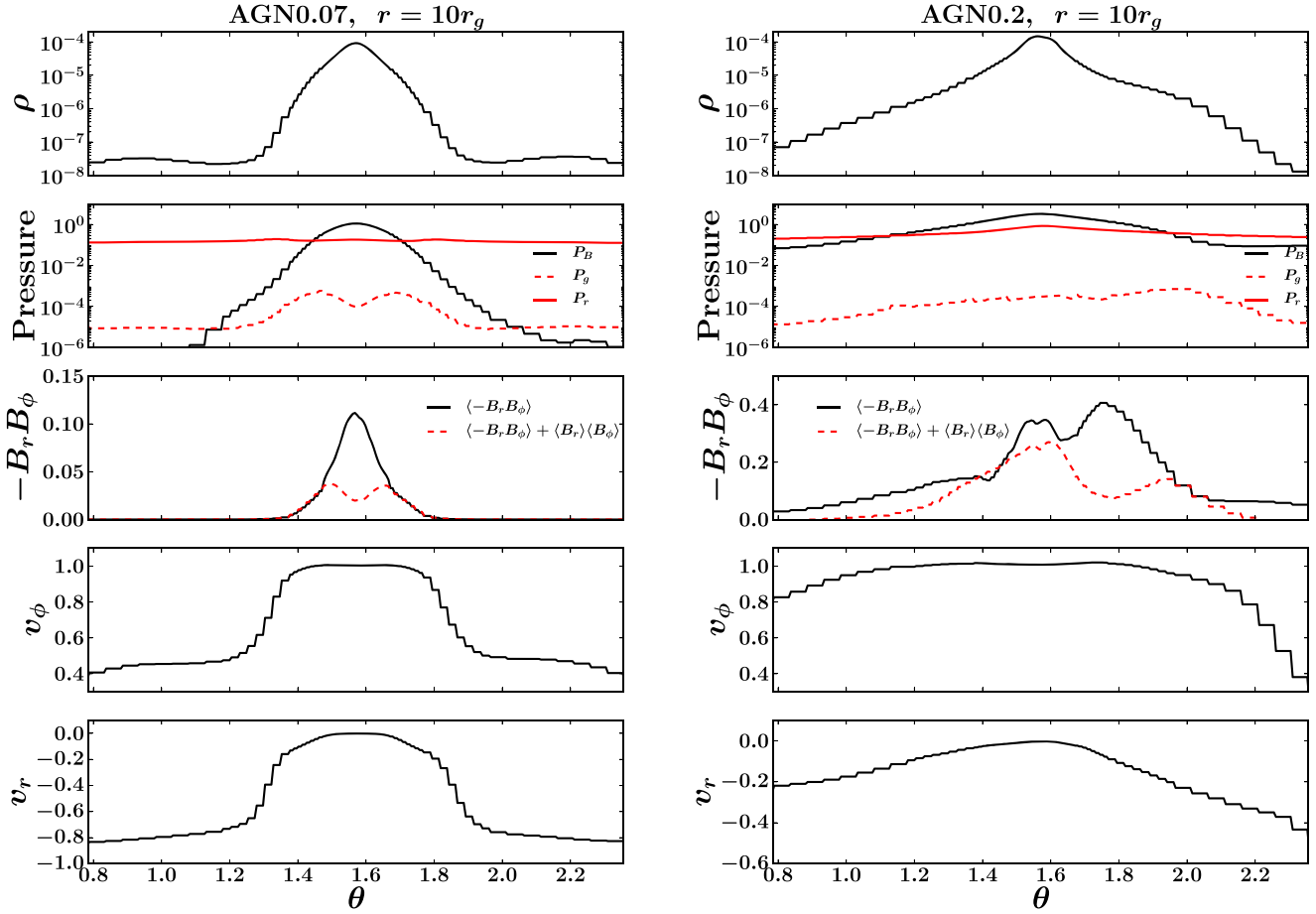

Figure 10. Time-averaged and azimuthally averaged vertical profiles of various quantities at $10r_g$ for the runs AGN0.07 left panels) and AGN0.2 right panels). From top to bottom, these quantities are density ρ in the top panel, gas P_g, dashed red lines), radiation P_r, solid red lines), and magnetic P_B, solid black lines) pressure in the second panel, total Maxwell stress solid black lines) as well as the turbulent component dashed red lines) in the third panel, density-weighted rotation fourth panel), and radial velocities bottom panel). Density is in units of ρ_0 while pressure and Maxwell stress are in units of P_0. The velocities are scaled with the Keplerian value at the midplane $\sqrt{rGM_{\rm BH}}/(r-2r_g)$.

Hirose et al. 2006, 2009; Jiang et al. 2016, 2019). Although the shell-averaged radiation pressure is comparable to the shell-averaged magnetic pressure in the run AGN0.07 Figure 4), the radiation pressure is relatively at with height and the whole disk is supported by the magnetic pressure gradient. In fact there is a small enhancement of P_r near the photosphere see also Figure 3) due to the significant radiation viscosity there. In the run AGN0.2, radiation pressure partially supports the disk near the midplane and the disk becomes completely supported by magnetic pressure around 10° away from the midplane. This also causes the density to drop more slowly with height around the same location, as shown in the right panel of Figure 10. Gas pressure is always smaller than the other pressure components by more than a factor of 1000.

For the two magnetic field configurations used in the simulations, besides the Maxwell stress from the turbulence, there are always significant azimuthally averaged mean $\langle B_r \rangle$ and $\langle B_\phi \rangle$, although the product of these components never becomes the dominant stress Figure 7). This is different from the magnetic pressure-supported disk as found by Gaburov et al. 2012), where the Maxwell stress is primarily due to $-\langle B_r \rangle \langle B_\phi \rangle$. Such disks also have different vertical distributions compared with the turbulent stress as shown in the third panels of Figure 10. The Maxwell stress generated by the turbulence the dashed red lines) shows double peaks away from the midplane, which is consistent with previous simulations Blaes et al. 2011; Jiang et al. 2016). The stress due to the azimuthally averaged mean magnetic field the difference between the solid black lines and the dashed red lines) is peaked at the midplane and drops quickly with height.

Inside the photosphere near the midplane, the rotation speed of the disk is pretty close to the Keplerian value with negligible radial in ow speed the fourth and bottom panels of Figure 10). Inside the coronal region, the rotation speed drops to only 40 of the Keplerian value and significant radial velocity is present.

Despite the fact that the disk is supported by magnetic pressure, the energy dissipated in the disk is transported vertically outward by both the radiation ux and Poynting ux near the midplane. Vertical profiles of the poloidal components of the energy uxes at $10r_g$ for the run AGN0.07 are shown in Figure 11. We have scaled these with the critical energy ux $F_c \equiv cGM_{\rm BH}|\cos(\theta)|/(\kappa_{\rm es}(r-2r_g)^2)$, which is the radiation ux if the vertical component of gravity were completely balanced by the radiation force with the electron scattering opacity $\kappa_{\rm es}$. The radiation ux is less than ≈5 of the critical value inside the disk, which confirms that radiation pressure plays a negligible role in supporting the disk. But the radiation ux is comparable to the Poynting ux within ≈3° away from the midplane and it completely dominates the energy transport beyond that. The sign of Poynting ux also suggests that

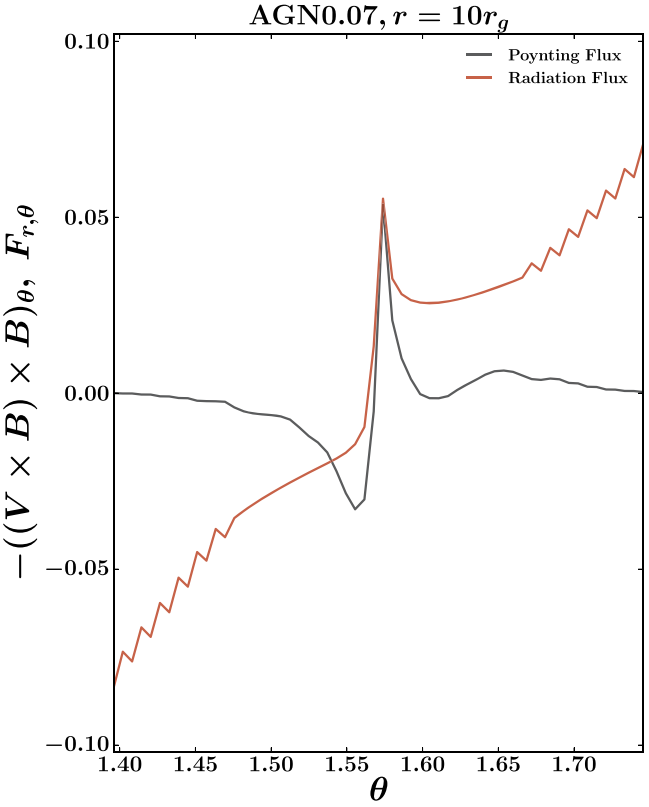

Figure 11. Time-averaged and azimuthally averaged vertical profiles of the poloidal components of Poynting ux black line) and radiation ux red line) at $10r_g$ for the run AGN0.07. The energy uxes are scaled with the critical value $cGM_{\rm BH}|\cos(\theta)|/(\kappa_{\rm es}(r-2r_g)^2)$.

magnetic energy amplified in the disk is transported away from the midplane likely due to magnetic buoyancy Blaes et al. 2011; Begelman et al. 2015), although this simulation does not show any butter y diagram Figure 2). The existence of nonzero azimuthally averaged radial magnetic field $\langle B_r\rangle$ in a localized region of the disk will also keep generating B due to the differential rotation of the disk, which is balanced by the buoyant escape of the field. Since the shell-averaged B_r is zero, B generated at different locations in the disk will reconnect and cause dissipation.

3.6. Properties of the Coronae

MHD simulations such as those presented here cannot capture the plasma physics of collisionless reconnection, nor do we include pair production, and both of these processes are likely happening in the coronae of real AGNs Fabian et al. 2015). Nevertheless, our simulations may be able to inform us as to the fraction of accretion power that is transferred into optically thin regions outside the disk photospheres. In our simulations this power is dissipated numerically at the grid scale and heats up the gas, and whether this fully happens in reality will require more detailed modeling of the microphysics. However, the simulations should be modeling reasonably accurately the fraction of power transferred to optically thin regions, and how this fraction changes with accretion rate in the disk and distance to the black hole. This contrasts with early models of coronae, where the fraction of power dissipated outside the disk is simply a free parameter Svensson & Zdziarski 1994; Zdziarski et al. 1999).

Local shearing box radiation MHD simulations Jiang et al. 2014b) have found that coronae with high gas temperature are only formed above the disk when the surface density is low enough that a significant fraction of the total dissipation happens in optically thin regions. For the surface density at $30r_g$ adopted by Jiang et al. 2014b) based on the standard thin-disk model, only 3.4 of the dissipation happens in the coronal region. This fraction is increased to more than 50 inside $15r_g$ for the run AGN0.07, with significantly reduced surface density in the magnetic pressure-supported disk. This results in a high gas temperature of $\approx 10^8$–10^9 K covering all the radial range $\lesssim 15r_g$ with height $20r_g$ away from the disk midplane, as shown in the left panel of Figure 12. When the accretion rate is increased to $26\%\dot{M}_{\rm Edd}$ in the run AGN0.2, the disk becomes thicker and the fraction of accretion as well as the associated dissipation in the optically thin region are also reduced. Coronae with high gas temperature $\gtrsim 10^8$ K) only show up inside $\lesssim 10r_g$ when the surface density drops to a value such that $\kappa_R\Sigma$ 2 $\lesssim$ 100. Inside this region, the corona is also more vertically extended, covering more than $40r_g$ away from the disk midplane.

What we have labeled as "coronae" in these simulations exhibit properties that are consistent with some of the observationally inferred properties of AGN coronae. The simulations only produce high-temperature coronae gas temperature $>10^8$ K) inside $\approx 10r_g$ and the temperature decreases with increasing distance from the black hole. This is because the surface density of the disk increases with radius and the fraction of dissipation in the optically thin region drops, which is necessary to maintain the high temperature in the corona. This agrees with the constraints from both re ection and microlensing modeling of AGN coronae Chartas et al. 2009; Dai et al. 2010; Reis & Miller 2013; Jiménez-Vicente et al. 2015), which suggest that they are compact with roughly the same size as we find.

The surface density increases for the same region of the disk when the accretion rate increases from AGN0.07 to AGN0.2. This is in contrast to the standard thin-disk model, for which the surface density is inversely proportional to the mass accretion rate in the radiation pressure-dominated regime. In our simulations, where the surface density and mass accretion rate both increase together, the fraction of dissipation in the optically thin regime is reduced and the radial regime where the corona is formed is also smaller. This will result in a smaller ratio between X-ray luminosity from the corona and luminosity of the thermal emission from the disk. This might provide a physical mechanism to explain the observational fact that the optical to X-ray spectral index of AGNs gets harder as luminosity decreases Steffen et al. 2006; Just et al. 2007; Ruan et al. 2019).

4. Discussion

It is interesting to compare the structures of the disk produced by our simulations with proposed models of magnetic pressure-dominated disks in the literature. Pariev et al. 2003) modified the standard disk model by including a magnetic pressure component in the disk, which was assumed to be larger than the thermal pressure at all radii. Magnetic pressure was assumed to be vertically constant at each radius and to decrease with increasing radius following a power law, the slope of which was a free parameter. The strength of the magnetic field was also a free parameter in this model. The disk

structure in this model is very similar to that in the original -disk model, which predicts that the surface density is proportional to $1/\dot{M}$. This is clearly in contrast to what we find from the simulations. Begelman & Pringle 2007) proposed that the toroidal magnetic field should saturate to a level such that the associated Alfvén velocity is the geometric mean of gas isothermal sound speed c_s and Keplerian speed V_k. Under this assumption, the disk surface density is found to be proportional to $\dot{M}^{7/9}$, which has the same sense as what we find, although their dependence on $\dot{M}$ is weaker. The Alfvén velocity in our simulations is found to be larger than $\sqrt{c_s V_k}$ by a factor of 2–3 in the midplane and much smaller than that near and above the photosphere. Our simulation results can be used to constrain the assumptions and improve these analytical models.

The relatively uniform spatial distribution of E_r in the run AGN0.07 is caused by the significant dissipation near the photosphere. In fact, E_r near the photosphere is slightly larger than E_r at the midplane, as shown in the left panel of Figure 10. This is also consistent with the rapid increase in radiation ux at these locations, as shown in Figure 11. For comparison, when more dissipation happens in the optically thick part of the disk, as in the run AGN0.2, the radiation energy density decreases with increasing height monotonically. This is also the reason why radiation viscosity can be significant in the run AGN0.07. Since radiation viscosity is proportional to E_r/τ in the optically thick regime, if E_r at the photosphere is smaller than E_r in the midplane by a factor of 1 τ as in the standard thin-disk model, then radiation viscosity will not be significant near the photosphere even though the mean free path is larger there.

These simulations adopt the gray approximation for radiation transport, and Compton scattering is included based on the effective radiation temperature to roughly estimate the energy exchange between photons and gas. This latter approximation will underestimate the gas temperature in the coronal region. Processes such as collisionless reconnection and pair production, which are important in determining the spectral properties of real coronae, are also not included in our simulations. Therefore, we cannot produce the expected spectra from these simulations directly. We have developed a Monte Carlo code to post-process the simulation data and generate spectra from the disk. Preliminary results show that the coronae in these simulations are indeed able to produce significant X-ray emission with X-ray luminosity consistent with the total dissipation we have in these region. Detailed properties of the emergent spectrum will be presented in a separate publication.

It is worthwhile noting that the density of the photosphere in our simulations $\approx 10^{-13}$ g cm $^{-3}$) is several orders of magnitude smaller than the typical value $10^{-7}-10^{-9}$ g cm $^{-3}$) adopted in lamppost models of the spectrum of X-rays re ected from accretion disks e.g., García et al. 2016). Such models assume that the density in the disk atmosphere is constant and the ionization structure is determined by a single ionization parameter. For electron scattering opacity, this high density at the photosphere would also imply a disk scale height only 10^{-7}–10^{-5} times the gravitational radius for a 5×10^{8} solar mass black hole, which is much smaller than what we find in our simulations. This high density is required in the lamppost model with a single ionization parameter to prevent the disk from being fully ionized so that the observed Fe K line profile can be reproduced. However, when more extended corona and disk structures are considered based on general relativistic MHD simulations Kinch et al. 2016), similar line profiles can also be generated with a density of the photosphere close to what we find. Finite disk thickness is also found to have interesting effects on the re ected line profiles Taylor & Reynolds 2018a, 2018b). Calculating the Fe K profile with coronal structures given by our simulations will be a necessary next step to test these simulation results.

The total luminosity from the inner $10r_g$ of the disk is only $1\%L_{\rm Edd}$ with $\dot{M}_{\rm Edd}=7\%\dot{M}_{\rm Edd}$ for the run AGN0.07, which means the radiative efficiency is only 1.4 . The radiative efficiency is slightly increased to $\approx$3.5 for the run AGN0.2. The efficiency from these disks is significantly smaller than the prediction of standard thin disks for the same radial range. One reason for the lower efficiency is the significant dissipation in the optically thin region, which cannot convert to thermal radiation efficiently. Another reason for the lower radiative efficiency in the run AGN0.07 is the stress—$\langle\langle B_r\rangle\rangle\langle\langle B_\phi\rangle\rangle$ near the disk midplane Figure 10). This component of stress can cause mass accretion without dissipation. No significant out ow is observed in the simulations despite strong magnetic pressure support in the disk.

Both of the simulations in this paper established long-lived thermal equilibria between turbulent dissipation of gravitational binding energy in the ow and radiative cooling. This is despite the fact that radiation dominates the thermal pressure, a situation that generally leads to thermal instability in -disk models Shakura & Sunyaev 1976), at least when electron scattering dominates the Rosseland mean opacity. Iron opacity can be significant in disks around supermassive black holes, and has been shown to stabilize the thermal instability in shearing box simulations of MRI turbulence Jiang et al. 2016). However, while we have included this source of opacity in the simulations here, it actually does not play a significant role in the inner regions near the black hole. Instead, it is likely that the fact that these simulations are supported by magnetic, not thermal pressure, leads to their stability Begelman & Pringle 2007). Indeed, Sadowski 2016) found that global simulations of geometrically thin disks are stabilized if the magnetic pressure exceeds half the total pressure, a criterion that we more than satisfy in our simulations here.

Light curves of a variety of accretion-powered sources in astrophysics, including AGNs, show a linear relationship between rms variability amplitude and ux see, e.g., Uttley et al. 2005 and references therein). There is a hint of this in the AGN0.2 light curve shown in Figure 1, where the variability amplitude is clearly larger at higher luminosities than at lower luminosities. Unfortunately, the simulation was not run long enough and the light curve is too short to produce a clean rms– ux relation. On the other hand, there is no indication of any relationship between variability amplitude and ux in AGN0.07. Hogg & Reynolds 2016) have suggested that the rms– ux relation is related to the presence of the characteristic butter y diagram of quasi-periodic azimuthal field reversals. It is therefore noteworthy that these are present only in AGN0.2, and not in AGN0.07 because of its much stronger magnetic pressure support. The presence of an rms– ux relation may be a way of observationally ruling out magnetic fields that are so strong that the butter y dynamo is suppressed, but longer simulations will need to be run to confirm this.

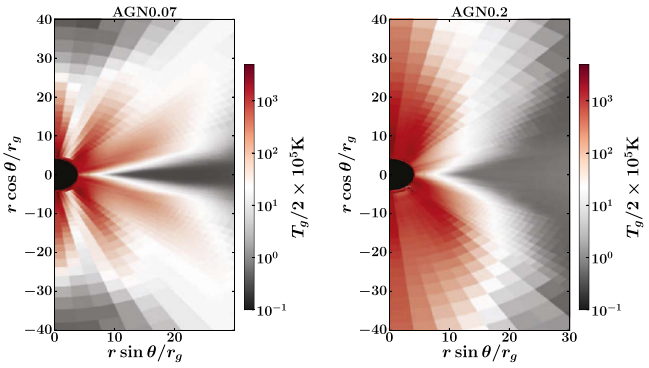

Figure 12. Time-averaged and azimuthally averaged spatial distributions of gas temperature T_g for the two runs AGN0.07 left panel) and AGN0.2 right panel). The gas temperature is $\approx$ 1–2) $\times$ 10^5 K in the optically thick part of the disk but increases to 10^8–10^9 K rapidly in the optically thin coronal regions.

Note that the shape and magnetic field in the initial tori we use for the two simulations AGN0.07 and AGN0.2 are very similar to the ones adopted by Jiang et al. 2019). We only changed the density of the torus to achieve different mass accretion rates, while the ratio between the initial magnetic pressure and radiation pressure was kept fixed. However, the accretion disks with super-Eddington accretion rates shown in Jiang et al. 2019) do not evolve to a magnetic pressure-dominated regime. When the surface density as well as the optical depth is increased, radiation pressure becomes more important in supporting the disk. Since the amount of magnetic field in the disk is determined by a balance between buoyant escape and amplification by the MRI, this suggests that stronger radiation support in the disk may either increase the magnetic buoyancy or reduce the saturation amplitude of MRI Jiang et al. 2013b). We intend to investigate this further in future work.

5. Summary

We have successfully simulated two accretion disks around a $5\times10^8M_{\rm BH}$ black hole with mass accretion rates reaching $0.07\dot{M}_{\rm Edd}$ and $0.2\dot{M}_{\rm Edd}$ up to $\sim15r_g$. The disks do not show any sign of thermal instability over many thermal timescales. The structure of the disk differs markedly from the standard thin-disk model Shakura & Sunyaev 1973) for the same mass accretion rate in the following ways.

1. The disk is supported vertically by magnetic pressure rather than thermal pressure for these accretion rates.
2. The surface density and total optical depth are reduced by a factor of $\approx$10. The disk scale height increases with radius significantly instead of being constant.
3. A significant fraction of dissipation as well as the associated mass accretion more than 50 for $\dot{M}=0.07\dot{M}_{\rm Edd}$) happens away from the disk midplane in the optically thin region, resulting in a high-temperature corona inside $10r_g$. The fraction of dissipation in the coronal region decreases with increasing mass accretion rate.
4. The transport of angular momentum is due to Maxwell and Reynolds stress inside the photosphere. But near the photosphere, radiation viscosity is the dominant mechanism for angular momentum transport, and this can dominate the vertically averaged stress.

We thank Julian Krolik for helpful comments on an earlier draft. We also thank the referee, Chris Reynolds, for useful suggestions that improved the paper significantly. This research was supported in part by the National Science Foundation under grant No. NSF PHY-1125915, 17-48958 and AST-1333091. S.W.D. is supported by a Sloan Foundation Research Fellowship. An award of computer time was provided by the Innovative and Novel Computational Impact on Theory and Experiment INCITE) program. This research used resources of the Argonne Leadership Computing Facility, which is a DOE Office of Science User Facility supported under Contract DE-AC02-06CH11357. Resources supporting this work were also provided by the NASA High-End Computing HEC) Program through the NASA Advanced Supercomputing NAS) Division at Ames Research Center. The Center for Computational Astrophysics at the Flatiron Institute is supported by the Simons Foundation.

ORCID iDs

Yan-Fei Jiang) https: orcid.org 0000-0002-2624-3399

References

Antonucci, R. 2013, Natur, 495, 165
Bai, X.-N., & Stone, J. M. 2013, ApJ, 767, 30
Begelman, M. C., Armitage, P. J., & Reynolds, C. S. 2015, ApJ, 809, 118
Begelman, M. C., & Pringle, J. E. 2007, MNRAS, 375, 1070
Begelman, M. C., & Silk, J. 2017, MNRAS, 464, 2311
Bisnovatyi-Kogan, G. S., & Blinnikov, S. I. 1976, SvAL, 2, 191
Blaes, O., Hirose, S., & Krolik, J. H. 2007, ApJ, 664, 1057
Blaes, O., Krolik, J. H., Hirose, S., & Shabaltas, N. 2011, ApJ, 733, 110
Chartas, G., Kochanek, C. S., Dai, X., Poindexter, S., & Garmire, G. 2009, ApJ, 693, 174
Dai, X., Kochanek, C. S., Chartas, G., et al. 2010, ApJ, 709, 278
Das, U., Begelman, M. C., & Lesur, G. 2018, MNRAS, 473, 2791
Davis, S. W., Stone, J. M., & Pessah, M. E. 2010, ApJ, 713, 52
Davis, S. W., Woo, J.-H., & Blaes, O. M. 2007, ApJ, 668, 682
Dexter, J., & Begelman, M. C. 2019, MNRAS, 483, L17
Fabian, A. C., Lohfink, A., Kara, E., et al. 2015, MNRAS, 451, 4375
Fragile, P. C., Etheridge, S. M., Anninos, P., Mishra, B., & Kluźniak, W. 2018, ApJ, 857, 1
Fragile, P. C., & Sadowski, A. 2017, MNRAS, 467, 1838
Frank, J., King, A., & Raine, D. J. 2002, Accretion Power in Astrophysics: Third Edition Cambridge: Cambridge Univ. Press)
Gaburov, E., Johansen, A., & Levin, Y. 2012, ApJ, 758, 103
García, J. A., Fabian, A. C., Kallman, T. R., et al. 2016, MNRAS, 462, 751
Haardt, F., & Maraschi, L. 1991, ApJL, 380, L51
Haardt, F., & Maraschi, L. 1993, ApJ, 413, 507
Hawley, J. F. 2001, ApJ, 554, 534
Hawley, J. F., Gammie, C. F., & Balbus, S. A. 1995, ApJ, 440, 742
Hawley, J. F., Guan, X., & Krolik, J. H. 2011, ApJ, 738, 84
Hawley, J. F., & Krolik, J. H. 2001, ApJ, 548, 348
Hirose, S., Krolik, J. H., & Blaes, O. 2009, ApJ, 691, 16
Hirose, S., Krolik, J. H., & Stone, J. M. 2006, ApJ, 640, 901
Hogg, J. D., & Reynolds, C. S. 2016, ApJ, 826, 40
Hogg, J. D., & Reynolds, C. S. 2018, ApJ, 854, 6
Honma, F., Matsumoto, R., & Kato, S. 1991, PASJ, 43, 147
Janiuk, A., Czerny, B., & Siemiginowska, A. 2002, ApJ, 576, 908
Jiang, Y.-F., Cantiello, M., Bildsten, L., Quataert, E., & Blaes, O. 2015, ApJ, 813, 74
Jiang, Y.-F., Davis, S. W., & Stone, J. M. 2016, ApJ, 827, 10
Jiang, Y.-F., Stone, J. M., & Davis, S. W. 2013a, ApJ, 778, 65
Jiang, Y.-F., Stone, J. M., & Davis, S. W. 2013b, ApJ, 767, 148
Jiang, Y.-F., Stone, J. M., & Davis, S. W. 2014a, ApJ, 796, 106
Jiang, Y.-F., Stone, J. M., & Davis, S. W. 2014b, ApJ, 784, 169
Jiang, Y.-F., Stone, J. M., & Davis, S. W. 2019, ApJ, 880, 67
Jiménez-Vicente, J., Mediavilla, E., Kochanek, C. S., & Muñoz, J. A. 2015, ApJ, 806, 251
Just, D. W., Brandt, W. N., Shemmer, O., et al. 2007, ApJ, 665, 1004
Kaufman, J., & Blaes, O. M. 2016, MNRAS, 459, 1790

Kinch, B. E., Schnittman, J. D., Kallman, T. R., & Krolik, J. H. 2016, ApJ, 826, 52
Kishimoto, M., Antonucci, R., Boisson, C., & Blaes, O. 2004, MNRAS, 354, 1065
Koratkar, A., & Blaes, O. 1999, PASP, 111, 1
Krolik, J. H., Hirose, S., & Blaes, O. 2007, ApJ, 664, 1045
Laor, A., & Davis, S. W. 2014, MNRAS, 438, 3024
Lightman, A. P., & Eardley, D. M. 1974, ApJL, 187, L1
Loeb, A., & Laor, A. 1992, ApJ, 384, 115
Masaki, I. 1971, PASJ, 23, 425
McKinney, J. C., Tchekhovskoy, A., Sadowski, A., & Narayan, R. 2014, MNRAS, 441, 3177
Mihalas, D., & Mihalas, B. W. 1984, Foundations of Radiation Hydrodynamics New York: Oxford Univ. Press)
Miller, K. A., & Stone, J. M. 2000, ApJ, 534, 398
Mishra, B., Begelman, M. C., Armitage, P. J., & Simon, J. B. 2019, arXiv:1907.08995
Mishra, B., Fragile, P. C., Johnson, L. C., & Kluźniak, W. 2016, MNRAS, 463, 3437
Morales Teixeira, D., Avara, M. J., & McKinney, J. C. 2018, MNRAS, 480, 3547
Noble, S. C., Krolik, J. H., & Hawley, J. F. 2009, ApJ, 692, 411
Ohsuga, K. 2006, ApJ, 640, 923
O Neill, S. M., Reynolds, C. S., Miller, M. C., & Sorathia, K. A. 2011, ApJ, 736, 107
Paczy sky, B., & Wiita, P. J. 1980, A&A, 88, 23
Pariev, V. I., Blackman, E. G., & Boldyrev, S. A. 2003, A&A, 407, 403
Paxton, B., Cantiello, M., Arras, P., et al. 2013, ApJS, 208, 4
Pessah, M. E., & Psaltis, D. 2005, ApJ, 628, 879
Piran, T. 1978, ApJ, 221, 652
Reis, R. C., & Miller, J. M. 2013, ApJL, 769, L7
Ruan, J. J., Anderson, S. F., Eracleous, M., et al. 2019, ApJ, 883, 76
Sádowski, A., & Narayan, R. 2016, MNRAS, 456, 3929
Salvesen, G., Armitage, P. J., Simon, J. B., & Begelman, M. C. 2016a, MNRAS, 460, 3488
Salvesen, G., Simon, J. B., Armitage, P. J., & Begelman, M. C. 2016b, MNRAS, 457, 857
Sadowski, A. 2016, MNRAS, 459, 4397
Schnittman, J. D., Krolik, J. H., & Noble, S. C. 2013, ApJ, 769, 156
Shafee, R., McKinney, J. C., Narayan, R., et al. 2008, ApJL, 687, L25
Shakura, N. I., & Sunyaev, R. A. 1973, A&A, 24, 337
Shakura, N. I., & Sunyaev, R. A. 1976, MNRAS, 175, 613
Shibata, K., Tajima, T., & Matsumoto, R. 1990, ApJ, 350, 295
Shull, J. M., Stevans, M., & Danforth, C. W. 2012, ApJ, 752, 162
Simon, J. B., Beckwith, K., & Armitage, P. J. 2012, MNRAS, 422, 2685
Sincell, M. W., & Krolik, J. H. 1997, ApJ, 476, 605
Socrates, A., Davis, S. W., & Blaes, O. 2004, ApJ, 601, 405
Sorathia, K. A., Reynolds, C. S., Stone, J. M., & Beckwith, K. 2012, ApJ, 749, 189
Steffen, A. T., Strateva, I., Brandt, W. N., et al. 2006, AJ, 131, 2826
Stone, J. M., Hawley, J. F., Gammie, C. F., & Balbus, S. A. 1996, ApJ, 463, 656
Svensson, R., & Zdziarski, A. A. 1994, ApJ, 436, 599
Taylor, C., & Reynolds, C. S. 2018a, ApJ, 855, 120
Taylor, C., & Reynolds, C. S. 2018b, ApJ, 868, 109
Tilton, E. M., Stevans, M. L., Shull, J. M., & Danforth, C. W. 2016, ApJ, 817, 56
Turner, N. J. 2004, ApJL, 605, L45
Uttley, P., Cackett, E. M., Fabian, A. C., Kara, E., & Wilkins, D. R. 2014, A&ARv, 22, 72
Uttley, P., McHardy, I. M., & Vaughan, S. 2005, MNRAS, 359, 345
Weinberg, S. 1971, ApJ, 168, 175
Yuan, F., & Narayan, R. 2014, ARA&A, 52, 529
Zdziarski, A. A., Lubi ski, P., & Smith, D. A. 1999, MNRAS, 303, L11
Zheng, W., Kriss, G. A., Telfer, R. C., Grimes, J. P., & Davidsen, A. F. 1997, ApJ, 475, 469
Zhu, Z., & Stone, J. M. 2018, ApJ, 857, 34